Fatigue Assessment of Suspension Bridges under Non-Stationary Buffeting Using TSD-RFC Method

Xinqi Zhang1[a*] 0000-0003-4873-2932

[a] School of Civil Engineering, Chongqing Jiaotong University, Chongqing 400074, China. Email: 971895608@qq.com

* Corresponding author

Abstract

Suspension bridges are subject to significant stress cycles over their operational lifespan due to wind loads, leading to fatigue damage. Traditional rainflow counting methods have limitations when applied to non-stationary wind loads, particularly when the stress response exhibits significant state changes, which can result in incomplete cycle identification or amplitude misjudgment. This paper proposes a Time-Domain-State Dual-Layer Rainflow Counting (TSD-RFC) method to address these shortcomings in fatigue analysis of suspension bridges under non-stationary wind loads. The method decomposes the non-stationary response signal into multiple quasi-stationary segments, applying the classical three-point rainflow counting method within each segment to identify primary fatigue cycles. Additionally, for state transition segments in the response, an independent state transition cycle counting layer is used to identify additional large-amplitude stress cycles induced by wind speed fluctuations. Comparison with traditional rainflow counting shows that the TSD-RFC method more accurately identifies stress cycles, particularly in high-amplitude stress regions, effectively distinguishing cycles caused by state transitions. In the fatigue assessment of suspension bridges, the TSD-RFC method results in approximately 11.39% higher fatigue damage than traditional methods at a wind speed of 20 m/s, demonstrating the significant advantages of this method in fatigue damage evaluation under non-stationary wind loads.

Keywords

Suspension Bridge, Non-Stationary Buffeting, Fatigue Assessment, Rainflow Counting Method.

1 Introduction

Large-span bridges are continuously subjected to natural wind excitation throughout their operational lifespan. As a result, the structural components accumulate numerous stress cycles due to wind-induced vibrations, making fatigue damage a key factor influencing the durability and service safety of these bridges(Banday et al., 2025; Thalla and Stiros, 2018). Ding explored the influence of wind direction on the fatigue damage and lifespan of Jiubao Bridge hangers. By integrating wind field data from a structural health monitoring system, a fatigue damage model was developed, considering both wind speed and direction, to assess the hangers' durability(Ding et al., 2025). Yuan presented a fatigue life evaluation framework for the suspender system of continuous suspension bridges, incorporating wind, traffic loads, and displacement-controlled devices (DCD). The results indicate that the absence of DCD accelerates fatigue damage, with long suspenders more affected by wind and short suspenders by traffic loads(Yuan et al., 2025). Wang analyzed the fatigue life of Qiao Jia-fan 2# Bridge, considering temperature and static wind loads. Results show the maximum stress occurs near the 0# block, with corrugated steel webs having significantly longer fatigue life than concrete(Wang and Jia, 2024). Allard assessed buffeting-induced fatigue damage in a suspension bridge under the Worst-case climate scenario RCP8.5, considering location and climate effects over 100 years(Allard and Snaiki, 2024). Yuan developed a fatigue analysis framework for continuous suspension bridges with displacement-controlled suspenders (DCS), showing that DCS improves fatigue performance by enhancing stiffness and load-bearing capacity, especially under traffic loads(Yuan, 2025). Su analyzed the wind-induced stress response of an asymmetric steel arch bridge with inclined ribs, identifying critical fatigue-prone areas and influential factors for hanger stress distribution under varying wind directions(Su, 2022). Unlike extreme wind-induced vibrations that occur during limit state conditions, fatigue failure is typically governed by moderate winds that act repetitively over a long period. Therefore, accurately characterizing the cyclic characteristics of wind-induced responses is critical for fatigue assessment.

Mountain wind fields often exhibit non-stationary characteristics, Su investigated two strategies for analyzing turbulence characteristics of non-stationary wind events in mountain valleys using high-frequency wind data, offering insights for wind engineering and fluid-structure interactions(Su, 2025). Pei developed a wind speed prediction model (WT-CNN-LSTM) combining wavelet decomposition, LSTM, and CNN, improving accuracy in mountainous areas by reducing MAE, MSE, and RMSE, offering insights for engineering applications(Pei et al., 2024). Jun compared non-stationary and stationary wind speed models, showing that the non-stationary model provides more accurate turbulence intensity, gust factor, and PSD, offering insights for mountainous wind speed analysis(Jun et al., 2025). Li's study investigated the effects of oncoming wind speed on a long-span bridge in a mountain valley, showing that higher wind speeds reduce turbulence intensity and increase wind attack angles, impacting bridge safety(Li et al., 2024). Non-stationary wind loads lead to larger structural responses(Zhang et al., 2025; Zhou et al., 2024), thereby increasing the fatigue damage to the structure. Hu proposed a fatigue evaluation method for steel truss suspension bridges under non-stationary and non-Gaussian buffeting, showing mid-span cables suffer the greatest fatigue and damage increases when both effects are considered(Hu et al., 2025). Therefore, wind-induced buffeting of suspension bridges in mountainous areas must consider non-stationary winds. Since the resulting structural response is strongly time-varying, accurately evaluating fatigue damage from non-stationary response histories is essential.

The rainflow counting method is the most commonly used cyclic identification technique in fatigue analysis; Chen proposed a probabilistic fatigue life prediction framework using piecewise stochastic rainflow counting and uncertain material properties, validated experimentally, showing loading randomness and mean stress models significantly influence fatigue life(Chen et al., 2020). Huang proposed a one-stage four-point rainflow algorithm using preprocessing, achieving 42% higher efficiency without accuracy loss, and enabling faster fatigue life estimation in structural health monitoring(Huang et al., 2023). Bibbo proposed a multiaxial rainflow counting method using a modified three-point ASTM algorithm and minimum circumscribed circle approach, showing good agreement with existing methods on simulated and experimental data(Bibbo et al., 2023). Obermayr presented a real-time online rainflow counting algorithm

for ECUs that considers power-on-time, reduces memory and computation demands, and enables large-scale load cycle identification(Obermayr et al., 2021). Wang developed critical-plane-based multiaxial cycle counting algorithms by modifying rainflow and range methods, achieving fatigue life predictions consistent with experimental results under random loading(Wang et al., 2019). However, when the structural response exhibits strong non-stationarity, directly applying the traditional rainflow counting method leads to distorted cycle distributions and biased damage estimation.

This study proposes a time-domain-state dual-layer rainflow counting method for non-stationary random wind loads. The non-stationary response is divided into several stationary segments, and the primary fatigue cycles within each segment are identified. Additionally, transition cycles occurring when the mean wind speed shifts between different segments are recognized. Using this framework, the fatigue damage of a suspension bridge subjected to non-stationary wind loading is investigated.

It should be noted that the proposed framework is fundamentally different from conventional piecewise rainflow counting approaches. Existing segmented methods mainly divide the signal into fixed local windows for local cycle counting or loading-spectrum reconstruction. In contrast, the segmentation adopted in the present study is not artificially prescribed, but is determined according to the quasi-stationary statistical characteristics of the non-stationary response itself. Furthermore, the proposed method does not only perform cycle counting within stationary segments, but also establishes a Markov-chain-based state-transition framework to characterize additional macroscopic cycles induced by stochastic switching between different response states. Therefore, the proposed framework focuses on state-transition-driven cycle evolution in non-stationary stochastic processes rather than conventional local window decomposition.

2 Non-Stationary Rainflow Counting Method

The non-stationary wind field in mountainous areas exhibits distinct features such as sudden fluctuations, leading to significant non-stationary characteristics in the wind-induced stress response of suspension bridges. In traditional fatigue analysis, the rainflow counting method effectively identifies the primary cycles in stress time histories. However, its single-layer counting approach, applied to the entire time series, struggles to distinguish between the cycles in stationary phases and those during state transitions. This issue is particularly evident in transition intervals, such as wind speed surges or wind direction shifts, where cycle identification can be incomplete or lead to amplitude misjudgment. To address this, this section proposes a time-domain-state dual-layer rainflow counting method. The entire time history is divided into several quasi-stationary segments based on the definition of stationarity. Within each segment, classical rainflow counting is used to identify the primary cycles. For the non-stationary disturbances during transitions between segments, an independent "state transition cycle" counting layer is constructed. This method allows for a more refined decomposition and evaluation of fatigue damage.

2.1 Rainflow Counting Method

The rainflow counting method is a cycle identification technique based on a sequence of turning points. It decomposes any one-dimensional random response into several "upward-downward" or "downward-upward" closed cycles. The core idea is to compare the amplitudes of adjacent peaks and valleys in the time series and progressively pair them according to specific rules. Ultimately, this process yields the amplitude and mean value for each pair of cycles, enabling a unified representation of complex and irregular waveforms.

Given a stress time history $x(t)$, the first step is to extract all local extrema, forming a turning point sequence $\{X_1, X_2, \ldots, X_n\}$ arranged in chronological order, where X_i represents the local peaks or valleys. A commonly used criterion for identifying extrema is:

$$(x_{i-1} - x_i)(x_i - x_{i+1}) < 0 \tag{1}$$

Points that satisfy the criteria are referred to as turning points. Figure 1 shows the response time history and its

corresponding peak-valley extraction results, where the circles represent the turning points in sequence $\{X_i\}$.

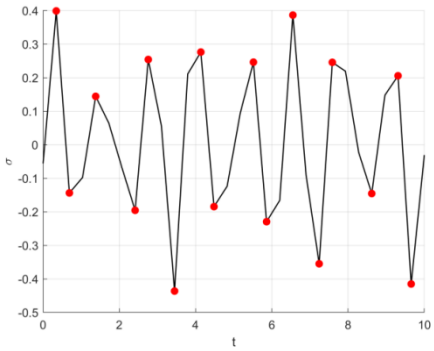

Figure 1: Response time history and the corresponding peak–valley extraction results

The three-point rainflow counting method is the most fundamental form of the rainflow algorithm. It determines whether a complete cycle is formed by comparing the relative amplitude magnitudes of any three consecutive turning points. For any three successive turning points X_{i-1}, X_i, and X_{i+1}, two adjacent amplitude differences are defined as:

$$\Delta_1 = |X_i - X_{i-1}| \tag{2}$$

$$\Delta_2 = |X_{i+1} - X_i| \tag{3}$$

The three-point rainflow cycle criterion is: $\Delta_1 \le \Delta_2$. Then the point pair (X_{i-1}, X_i) forms a complete cycle, and the corresponding cycle amplitude and mean value are given by:

$$A = \frac{|X_i - X_{i-1}|}{2} \tag{4}$$

$$M = \frac{X_i + X_{i-1}}{2} \tag{5}$$

After a cycle is identified, the corresponding turning-point pair is removed from the sequence, and the procedure continues iteratively until the entire sequence has been processed.

Through the above procedure, the amplitude–mean pairs $\{(A_k, M_k)\}_{k=1}^{N_c}$ of all closed cycles can be obtained. For subsequent fatigue damage or reliability analysis, the results are often summarized as a cycle counting matrix N_{pq} or presented in the form of a two-dimensional histogram. Several amplitude intervals $\{A_p\}$ and mean value intervals $\{M_q\}$ are selected and defined as:

$$N_{pq} = \{k \mid A_k \in [A_p, A_{p+1}), M_k \in [M_q, M_{q+1})\} \tag{6}$$

2.2 Time-Domain–State Dual-Layer Rainflow Counting Method

Under the action of a non-stationary wind field in mountainous areas, the response time history of a suspension bridge typically exhibits both slowly varying trends and abrupt changes. On the one hand, during certain periods the mean and variance remain approximately constant, which can be regarded as quasi-stationary segments. On the other hand, when wind speed or wind direction changes rapidly, the response mean rises or drops significantly, and additional large-amplitude cycles often occur in these transition segments. If the conventional rainflow counting method is applied directly to the entire non-stationary time history, all cycles will be mixed together, resulting in incomplete cycle identification and amplitude misjudgment. Therefore, based on the traditional rainflow counting introduced in Section 2.1, a time-domain–state dual-layer cycle identification framework is introduced to achieve a more accurate decomposition of non-stationary responses. Unlike conventional segmented rainflow counting methods, the proposed framework does not treat segmentation as a simple local windowing strategy. Instead, the non-stationary response is

first decomposed into statistically meaningful quasi-stationary states according to the evolution of local statistical characteristics. The switching behavior among different states is then modeled using a Markov-chain-based state-transition framework. Consequently, the proposed method distinguishes not only local cycles within stationary states, but also transition-induced macroscopic cycles generated by stochastic state evolution.

The basic idea of the method is as follows. First, according to the statistical characteristics of the response, the whole non-stationary response is divided into several response state segments that are approximately stationary in terms of mean and variance. Then, the three-point rainflow counting method is independently applied within each state segment to identify local cycles, yielding the intra-segment cycle set. Subsequently, each state segment is compressed into a representative upper–lower envelope extreme point to construct a state-mean sequence, and rainflow counting is performed again on this sequence to identify additional cycles caused by state transitions.

The resulting dual-layer cycle information preserves both the high-frequency small-amplitude cycles within non-stationary segments and the low-frequency large-amplitude cycles induced by wind-field switching, which facilitates subsequent evaluation of the fatigue effects of non-stationary responses on structural components. For clarity, let a certain response component be denoted as $x(t), \quad t \in [0, T_{\text{tot}}]$.

(1) General Non-Stationary Stochastic Process Model

Mathematical Characteristics of Non-Stationarity

Let $x(t)$ be a stochastic process defined over the interval $[0,T]$. Its first- and second-order statistical moments are respectively given by:

$$\mu(t) = \mathbb{E}[x(t)], \quad \sigma^2(t) = \mathbb{E}\left\{[x(t) - \mu(t)]^2\right\} \tag{7}$$

If the following conditions are satisfied:

$$\mu(t_1) \neq \mu(t_2) \ , \ \sigma^2(t_1) \neq \sigma^2(t_2) \tag{8}$$

Then the process is termed non-stationary. More generally, if the covariance:

$$R_x(t_1, t_2) = \mathbb{E}\left[x(t_1)x(t_2)\right] \tag{9}$$

If it does not depend solely on the time lag $|t_1 - t_2|$, the process is second-order non-stationary.

Many natural excitations (such as wind speed, traffic flow, ocean waves, and temperature variations) exhibit this characteristic, implying that their cyclic features are no longer generated by a single stationary process but instead consist of multiple statistical stages.

A general non-stationary process can be well approximated as a concatenation of several stationary processes along the time axis.

$$x(t) = \sum_{i=1}^{q} \left(m_i + \sigma_i y_i(t)\right) I\left(t \in \mathcal{S}_i\right) \tag{10}$$

where: $\mathcal{S}_i = [t_{i-1}, t_i]$ denotes mutually non-overlapping time intervals; $y_i(t)$ is a stationary process with zero mean and unit variance; m_i and σ_i are respectively the mean and standard deviation of the i-th segment; q is the number of segments; and $I(\cdot)$ is the indicator function.

Non-stationarity arises from abrupt or gradual variations of statistical properties over time. More generally, it can also be expressed in the spectral representation form:

$$x(t) = \sum_{i=1}^{q} \int_{-\infty}^{\infty} H_i(\omega) e^{j\omega t} dW_i(\omega), \quad t \in \mathcal{S}_i \tag{11}$$

This indicates that each segment possesses its own frequency structure. Regardless of the representation adopted, the central idea remains that a continuous non-stationary process is composed of a finite number of stationary processes. This forms the mathematical basis for the subsequent state construction, transition modeling, and the dual-layer rainflow counting method.

(2) Non-Stationary Segmentation and State Construction

To identify the stationary segments in Eq. (10) from the actual time history, this study adopts a strict definition of stationarity to segment the response record, i.e., the original time history is divided into several subsequences that can be regarded as stationary in a statistical sense. Within each subsequence, the mean and variance of the response should vary slowly with time or remain approximately constant, rather than fluctuate rapidly.

The specific procedure is as follows.

① Estimation of local statistical quantities

For the response $x(t)$, a moving window of length L is introduced, and the local mean and variance within the window are calculated as:

$$\mu(t)=\frac{1}{L}\int_{t}^{t+L}x(\tau)d\tau \tag{12}$$

$$\sigma^{2}(t)=\frac{1}{L}\int^{t+L}[x(\tau)-\mu(t)]^{2}d\tau \tag{13}$$

② Stationarity criterion

The local stationarity condition is defined as:

$$|\mu(t+L)-\mu(t)|\le\varepsilon_{\mu},\quad |\sigma(t+L)-\sigma(t)|\le\varepsilon_{\sigma} \tag{14}$$

where ε_{μ} and ε_{σ} denote the allowable thresholds for variations in the mean and variance, respectively. Continuous time intervals satisfying the above condition are regarded as stationary segments (state segments).

③ Non-stationary boundary identification

If the following situations occur, a state transition is considered to take place and segmentation is performed at that point: a sudden change in the mean $|\Delta\mu|>\varepsilon_{\mu}$, or a sudden change in the variance $|\Delta\sigma|>\varepsilon_{\sigma}$. The final result is $0=t_1^{\mathrm{beg}}<t_1^{\mathrm{end}}=t_2^{\mathrm{beg}}<\cdots<t_K^{\mathrm{end}}=T$, meaning the response is divided into K stationary subsections S_k. Each subsection can then be regarded as a statistical state.

(3) Markov Chain Modeling

Let the state evolution of the non-stationary process be represented by the sequence $S_1\to S_2\to\cdots\to S_q$. In the proposed framework, the introduction of the Markov chain is not merely for describing the state-switching process qualitatively. More importantly, it provides a quantitative mechanism for determining the residence behavior and transition intervals of different response states. Since transition-induced cycles must originate from actual state-switching regions in the original response history, identifying the representative transition interval is essential for constructing physically meaningful state-layer cycles. The Markov-chain-based residence-time distribution therefore serves as the theoretical basis for locating transition-cycle regions in the non-stationary response. When the transition rule of the state depends only on the current state and is independent of earlier historical states, the sequence satisfies the Markov property, and its conditional probability can be expressed as:

$$\Pr\{S_{k+1}=j|\ S_k=i,S_{k-1},\ldots\}=\Pr\{S_{k+1}=j|\ S_k=i\} \tag{15}$$

This assumption has clear physical and statistical foundations. First, each state $S_i=(m_i,\sigma_i)$ can fully characterize the main statistical features of the process within the corresponding time interval, such as the mean, variance, or energy distribution; therefore, the current state itself already contains the essential information required to describe future evolution. Second, state transitions in a non-stationary process are typically triggered by abrupt changes in external loads or system conditions, and such triggering mechanisms generally depend only on the current system state rather than on earlier history. Finally, the non-stationary behavior of many engineering systems exhibits finite memory, and the state transition mechanism can be effectively described by first-order conditional dependence.

Based on these considerations, the state sequence can be regarded as a first-order Markov chain. Since the number of states is finite, a transition matrix can be constructed. This transition matrix comprehensively characterizes the transition probabilities among different states, thereby providing a well-defined and quantifiable framework for modeling non-stationary processes.

Define the transition probability as:

$$\pi_{ij} = \Pr\{S_{k+1} = j \mid S_k = i\} \tag{16}$$

which forms the transition matrix:

$$\mathbf{P} = \begin{bmatrix} \pi_{11} & \pi_{12} & \cdots & \pi_{1m} \\ \pi_{21} & \pi_{22} & \cdots & \pi_{2m} \\ \vdots & \vdots & \ddots & \vdots \\ \pi_{m1} & \pi_{m2} & \cdots & \pi_{mm} \end{bmatrix} \tag{17}$$

where $\pi_{ij} \geq 0$ and $\sum_j \pi_{ij} = 1$ denote the states, and the state residence time T_i can be obtained from the length of S_i. The mean level of each state segment m_k, the jump amplitude between states $|m_{k+1} - m_k|$, and the back-and-forth switching process between states are precisely what generate the large-scale cycles in the non-stationary process.

The Markov chain matrix is derived from statistical analysis of the state sequence of the non-stationary response. First, based on the definition of stationarity, the original non-stationary sequence is divided into multiple stationary states to obtain the state sequence $y(k)$. Then, the actual number of transitions from state i to state j is counted to form the counting matrix F. By normalizing each row, the transition probability matrix $\mathbf{P}$ is obtained, i.e.,

$$p_{ij} = \frac{F_{ij}}{\sum_j F_{ij}} \tag{18}$$

The transition matrix describes the switching behavior of the non-stationary load among different states and constitutes the core of the Markov chain construction. It can be used not only to estimate the average residence time of each state, but also to directly obtain the number of transition cycles through the Markov–Rainflow method. In this way, the state transitions of the load are combined with fatigue cycles, enabling the establishment of a non-stationary rainflow counting model.

(4) Time-Domain–State Dual-Layer Rainflow Counting Method

Based on the above segmentation, state sequence, and switching structure, this section proposes a dual-layer cycle identification framework. The method classifies cycles into: Time-layer(intra-segment) cycles: cycles generated by the stationary process within each state segment; State-layer cycles: additional cycles caused by mean-value changes between different states, thereby providing a comprehensive characterization of the cyclic structure of the non-stationary process.

For the response sequence within each state segment S_i, the three-point rainflow counting method is performed to obtain the set of closed cycles of the locally stationary segment:

$$C_i^{\text{in}} = \left\{ \left(A_{i,r}^{\text{in}}, M_{i,r}^{\text{in}} \right) \mid r = 1, \ldots, N_i^{\text{in}} \right\} \tag{19}$$

where $A_{i,r}^{\text{in}}$ denotes the amplitude, $M_{i,r}^{\text{in}}$ represents the mean value, and N_i^{in} is the number of intra-segment cycles. All intra-segment cycles can be collectively expressed as:

$$C^{\text{in}} = \bigcup_{i=1}^{q} C_i^{\text{in}} \tag{20}$$

Take the mean value m_i of each state segment to construct the sequence:

$$y(k) = m_{S_k}, \quad k = 1, \ldots, q \tag{21}$$

Perform three-point rainflow counting on the sequence $y(k)$:

$$\left\{ \left(m_i^{\text{low}}, m_j^{\text{high}}, n_{ij}^{\text{rf}} \right) \right\} \tag{22}$$

These cycles represent the back-and-forth variation of the state mean level, i.e., the macroscopic cycles of the non-stationary process. Their characteristics are: they are generated by transitions between states and correspond to signals

with large amplitude and low frequency. At this stage, only the state-layer is used to determine which state pairs form cycles and their counts-equivalent to performing an abstract rainflow counting on the Markov state sequence-without directly yielding the actual response cycle amplitudes.

To relate the state-layer cycles to the real stress/displacement amplitudes, the Markov transition matrix $P=\left[p_{ij}\right]$ and the state residence-time information obtained in the previous subsection are required. For an arbitrary state i, when the system is in this state, the probability that it remains in state i in the next step is p_{ii}; therefore, the single continuous residence length L_i follows a geometric distribution:

$$P\left(L_i=\ell\right)=p_{ii}^{\ell-1}\left(1-p_{ii}\right),\quad \ell=1,2,\ldots \tag{23}$$

Its tail probability is given by:

$$P\left(L_i\geq n\right)=p_{ii}^{n-1} \tag{24}$$

It represents the probability that the process remains in state i for at least n sampling points. To ensure that the extracted extrema are representative, this study utilizes the tail probability property of the geometric distribution and sets the residence-length coverage probability to 95%, i.e., only extremely long residence durations with probability not exceeding 5% are regarded as tail events. The obtained residence-length bound can therefore be considered the typical time range for exiting a state, ensuring that the transition-cycle amplitudes originate from the state switching itself rather than from abnormal points caused by excessively long residence. Accordingly, the typical exit-window length of state i is determined from $p_{ii}^{n_i-1}=\varepsilon$.

$$n_i=1+\frac{\ln\varepsilon}{\ln p_{ii}} \tag{25}$$

Similarly, for entering state j, the entry-window length n_j can be obtained from p_{jj}. In this way, the typical range of state residence length is fully determined by the geometric distribution, avoiding subjective selection of the window size.

In constructing each state-layer transition cycle, the corresponding time interval is first determined using the state sequence $S(t)$. Suppose a transition from state i to state j occurs within the time interval $\left[t_i^-,t_i^+\right]\rightarrow\left[t_j^-,t_j^+\right]$; then, within the lower state segment i, only the tail portion is considered.

$$\Omega_i^-=\left[t_i^+-\min\left(L_i,n_i\right)+1,t_i^+\right] \tag{26}$$

Within this typical exit window, a representative valley is identified; within the high-state segment j, only the initial portion is considered.

$$\Omega_j^+=\left[t_j^-,t_j^-+\min\left(L_j,n_j\right)-1\right] \tag{27}$$

Within this typical entry window, a representative peak is identified, where L_i and L_j denote the actual residence lengths of the current stay. Let the original response be $x(t)$; then define:

$$v_i^*=\min_{t\in\Omega_i^-}x(t),\quad p_j^*=\max_{t\in\Omega_j^+}x(t) \tag{28}$$

Accordingly, the transition-cycle amplitude and mean value corresponding to this state switch are constructed as:

$$A_{ij}^{\mathrm{tr}}=p_j^*-v_i^*,\quad M_{ij}^{\mathrm{tr}}=\frac{p_j^*+v_i^*}{2} \tag{29}$$

The above procedure indicates that the state-layer rainflow counting consists of two steps: abstract counting and physical assignment. The former performs three-point rainflow counting on the state-mean sequence and, based on Eq. (22), determines the cyclic relationships and occurrence numbers between different state pairs. The latter uses the self-transition probabilities p_{ii} and p_{jj} in the Markov transition matrix to define the typical time scale of residence length. Within the window determined by the geometric distribution, local extrema closely associated with state switching are extracted from the original response, thereby obtaining transition-cycle amplitudes $\left(A_{ij}^{\mathrm{tr}},M_{ij}^{\mathrm{tr}}\right)$ with clear physical meaning. These transition cycles reflect the back-and-forth variation of the state mean level, i.e., the macroscopic cycles

of the non-stationary process. Their characteristics are that they are generated by transitions between states and correspond to signals with large amplitude and low frequency. Finally, the intra-segment cycles in the time layer and the switching cycles in the state layer together constitute the complete cycle structure:

$$\mathcal{C} = \mathcal{C}^{\text{in}} + \mathcal{C}^{\text{tr}} \tag{30}$$

The non-stationary process is decomposed into two types of cycle sources: small-scale cycles caused by turbulence within stationary segments and large-scale cycles induced by state transitions, thereby clearly distinguishing state-layer cycles from local-layer cycles. The Markov chain is used to establish the sequential structure of state switching, while rainflow counting identifies closed cycles from the sequence. The method is applicable to various non-stationary signals, including non-stationary wind-induced responses.

3. Numerical Examples

Under non-stationary random vibrations, fatigue cycles evolve over time, and their peak-valley sequences do not satisfy the stationarity assumption. Existing methods cannot directly obtain an accurate stress cycle distribution as a benchmark solution. Therefore, Example 1 presents an approximately stationary response by constructing conditions with sufficiently long stationary segments and minimal state transitions, making the overall response nearly stationary. In this case, the traditional rainflow counting method can be considered a benchmark solution. By comparing the proposed method with the traditional rainflow counting method, the accuracy of the dual-layer rainflow counting method can be verified.

Furthermore, Example 2 considers a constructed non-stationary stochastic response with pronounced time-varying statistical characteristics. The response sequence is generated by concatenating several stationary random processes with significantly different mean and variance characteristics according to a pre-defined state transition rule, thereby exhibiting evident non-stationarity and state-switching behavior. Under such conditions, the traditional rainflow counting method cannot distinguish local cycles within individual stationary segments from large-amplitude cycles induced by transitions between different statistical states. In contrast, the proposed method can separately identify the state transition cycles while simultaneously obtaining the complete cycle spectrum of the response. Through comparison of the two methods, the limitations of the traditional rainflow counting method in handling non-stationary processes, as well as the necessity and effectiveness of the proposed method, can be clearly demonstrated.

3.1 Fatigue Assessment of Approximate Stationary Response

To verify the accuracy of the time-domain–state dual-layer rainflow counting method proposed in this study, Example 1 constructs a typical weakly non-stationary response scenario. This scenario is formed by concatenating three stationary random processes in chronological order. The specific details are provided in Table 1:

Table 1. Information of Different Sub-segments of the Signal

Sub-segment	Time Interval	Mean	Variance	State Category
Sub-segment 1	0-250	0	1	1
Sub-segment 2	250-270	0.5	1.05	2
Sub-segment 3	270-600	0	1	1

As shown in the table, Sub-segment 1 and Sub-segment 3 have identical statistical characteristics (mean of 0 and standard deviation of 1), while Sub-segment 2 exhibits slightly higher mean and variance, which can be considered a short-term disturbance. The overall 600-second response formed by concatenating these three segments can still be approximately regarded as a stationary process. This construction allows the cycle results obtained by the traditional rainflow counting method to be used as a benchmark solution, thereby verifying the accuracy of the time-domain–state dual-layer rainflow counting method. The response signal time history and the mean step plot are shown in Figure 2.

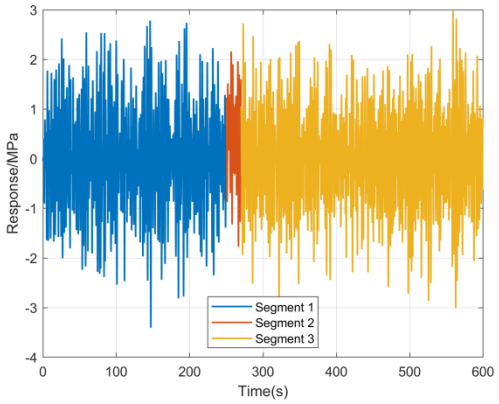

(a) Original response and its segmentation

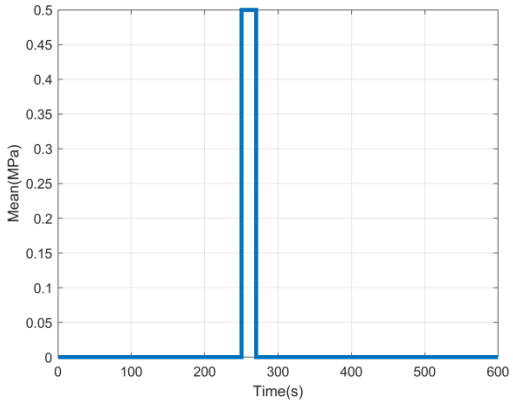

(b) Mean step plot for different sub-segments

Figure 2: Segmentation of Approximate Stationary Response

Figure 2 illustrates the segmentation of the approximate stationary response. (a) shows the original non-stationary response along with the three quasi-stationary segments obtained based on the definition of stationarity. (b) presents the stepwise representation of the mean values of the different sub-segments over time, providing an intuitive visual of the variation in mean levels between the segments.

The sampling frequency is 10Hz, and the length of the corresponding time history sequence is N=6000. Of these, state 1 occupies 5800 points, and state 2 occupies 200 points. From the perspective of a probabilistic model, this state sequence can be equivalently understood as a two-state chain: the response stays in state 1 for most of the time and only transitions briefly to state 2 during disturbances, before quickly returning to state 1. This behavior can be represented by constructing a counting matrix F using adjacent sample pairs in the state sequence. By traversing $S(t)$, the state count is determined, and the counting matrix is obtained as:

$$F=\begin{bmatrix} f_{11} & f_{12} \\ f_{21} & f_{22} \end{bmatrix}=\begin{bmatrix} L_1-1 & 1 \\ 1 & L_2-1 \end{bmatrix}=\begin{bmatrix} 5799 & 1 \\ 1 & 199 \end{bmatrix} \tag{31}$$

The total number of samples in state 1 is L_1, and the total number of samples in state 2 is L_2. Further normalization of the rows yields the state transition probability matrix corresponding to this example:

$$P=\begin{bmatrix} \dfrac{L_1-1}{L_1} & \dfrac{1}{L_1} \\ \dfrac{1}{L_2} & \dfrac{L_2-1}{L_2} \end{bmatrix}=\begin{bmatrix} 0.9998 & 0.0002 \\ 0.0050 & 0.9950 \end{bmatrix} \tag{32}$$

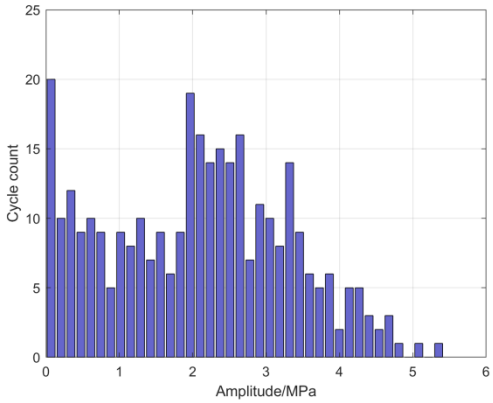

(a) Amplitude histogram

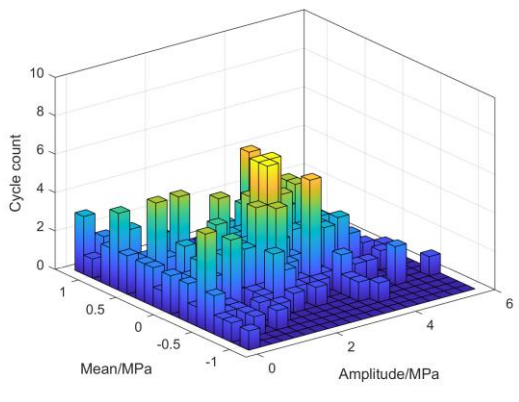

(b) Rainflow cycle diagram

Figure 3: Traditional Rainflow Counting Method

Figure 3 shows the cycle characteristic distribution obtained using the traditional three-point rainflow counting method for the concatenated approximate stationary response. The cycle amplitudes are primarily concentrated in the 0-3.5MPa range.

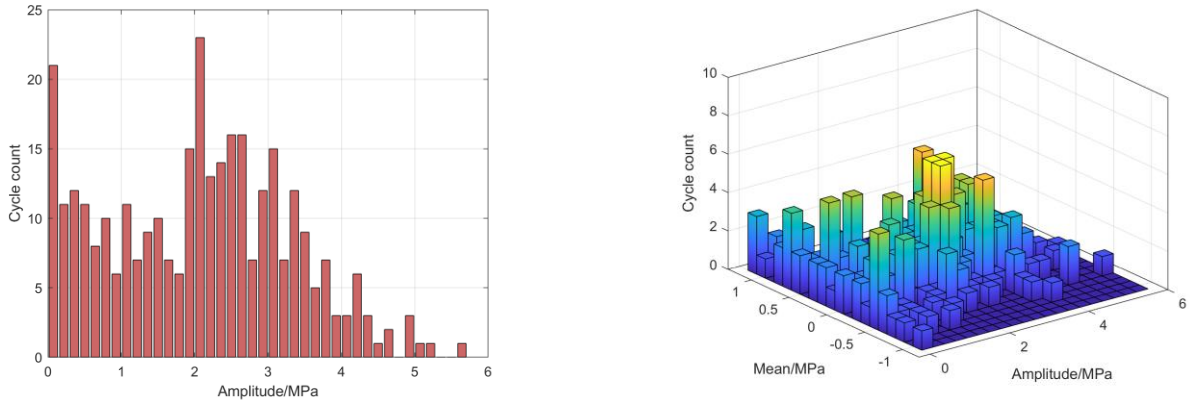

(a) Amplitude histogram (b) Rainflow cycle diagram

Figure 4: Dual-Layer Rainflow Counting Method

Figure 3 (a) and 4 (a) show similar distribution patterns for both methods, but there are slight differences in the cycle counts within the intervals. This difference is not due to the signal's randomness but rather because the dual-layer rainflow counting method treats the three segments as independent quasi-stationary segments, performing rainflow counting separately within each segment and independently identifying peaks and valleys. This segmentation alters some of the peak-valley matching relationships, causing small-value cycles that would have otherwise been paired across segments to be confined within each segment, resulting in slight variations in the small-cycle counts compared to the traditional method. This is an inherent difference in the algorithm between segmented and continuous rainflow counting. Additionally, in the high-amplitude region, the dual-layer method shows slightly higher values, as it accounts for additional stress cycles induced by state transitions, which typically have high amplitudes and low frequencies.

Figure 3 (b) and 4 (b) present the 3D rainflow cycle diagrams obtained from the traditional and dual-layer rainflow counting methods. Overall, the cycle counts in different intervals are largely consistent, with a concentration around the mean stress of zero, and a gradual decrease in cycle counts as the amplitude increases, reflecting the typical characteristics of narrowband random vibration. There are differences in the small- and high-amplitude ranges between the two methods, which are explained above.

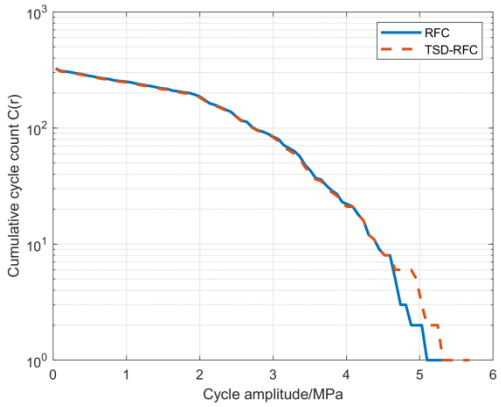

Figure 5: Comparison of Cumulative Stress Cycle Counts

Figure 5 compares the cumulative cycle count curves C(r) obtained from the traditional and the dual-layer rainflow counting methods. The two curves almost overlap over nearly the entire amplitude range, indicating a very high consistency in identifying cycles within the main fatigue-relevant region. In the small-amplitude range, the difference is negligible. As discussed previously, this slight deviation arises because the dual-layer method performs rainflow counting separately in quasi-stationary segments, slightly altering peak–valley matching and redistributing a small number of low-amplitude cycles. Since their quantity is extremely small relative to the total cycles, the effect is barely visible in the cumulative curve.

In the 4–5.5MPa range, the cumulative curve from the dual-layer method is slightly higher than that of the traditional method, with the difference concentrated in the tail. This is because the dual-layer rainflow counting method can identify additional large-amplitude transition cycles at state-switching points, whereas these cycles are typically absorbed by local peak–valley pairing in the traditional method and do not form independent large cycles. Although the difference is minor for approximately stationary conditions and has limited influence on the overall stress cycles, it demonstrates that the proposed method can capture state-transition effects that the traditional approach cannot explicitly represent.

After obtaining the stress cycles identified by both methods, their influence on structural fatigue performance must be quantified. A classical high-cycle fatigue model based on the S–N curve, combined with Miner's rule, is adopted to calculate the fatigue damage corresponding to each counting method and evaluate the engineering significance of their differences.

In this example, to facilitate comparison between different cycle counting methods, the material parameters are taken as $m=3$ and $C=1.0\times10^{12}$. The fatigue damage and corresponding fatigue life obtained from the two methods are calculated, and the fatigue contribution at different stress amplitudes is shown in Figure 6.

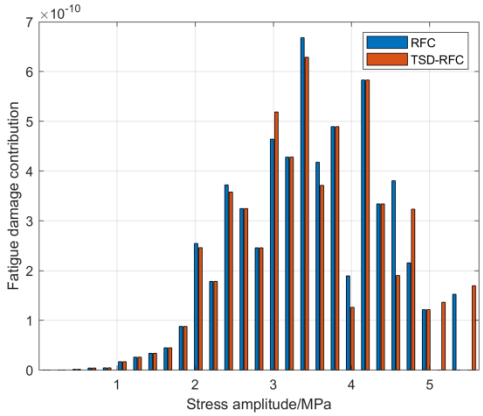

Figure 6: Comparison of Cumulative Stress Cycle Counts

Figure 6 shows the fatigue damage contributions obtained by the traditional rainflow counting method and the dual-layer rainflow counting method across different stress amplitude ranges. The overall damage distribution trends of the two methods are essentially consistent, verifying the accuracy of the proposed approach. Fatigue damage is mainly concentrated in the stress amplitude range of approximately 2.0–4.0MPa. The dual-layer rainflow counting method yields slightly higher fatigue contributions because it explicitly identifies transition cycles generated near state-switching points, which typically have relatively large stress amplitudes. However, under approximately stationary conditions, their overall proportion is low, resulting in a limited influence on total life-cycle damage. The fatigue damage and life predictions from both methods are summarized in Table 2.

Table 2. Fatigue Life Evaluation by Different Methods

Method	Fatigue Damage	Ratio	Fatigue Life	Variance
RFC	6.07×10^{-9}	1：1.006	1.648×10^{8}	1：0.992
TSD-RFC	6.11×10^{-9}		1.636×10^{8}	

Table 2 presents the total fatigue damage and the corresponding equivalent fatigue life obtained by the two methods. The damage ratio is approximately 1:1.006, and the life ratio is about 1:0.992, with differences within 1%. This indicates that, for the approximately stationary response constructed in this example, the traditional rainflow counting method can be regarded as an accurate benchmark solution, while the dual-layer rainflow counting method shows negligible deviation in both the overall cycle spectrum and fatigue damage evaluation, thereby confirming its accuracy and effectiveness.

The dual-layer rainflow counting method remains highly consistent with the benchmark solution without relying on global stationarity, demonstrating that it does not introduce significant additional computational error. This example verifies the computational accuracy of the TSD-RFC method and provides a reliable basis for subsequent analyses under typical non-stationary loading conditions.

3.2 Fatigue Assessment of Non-Stationary Response

To analyze the applicability of the proposed time-domain–state dual-layer rainflow counting method under typical non-stationary loading, this section constructs a non-stationary stochastic process with significant time-varying mean and variance characteristics. This scenario is formed by concatenating five stationary random processes with significantly different statistical characteristics in chronological order, resulting in a typical strongly non-stationary response sequence. The information for each subsegment is shown in Table 3.

Table 3. Fatigue Life Evaluation by Different Methods

Sub-segment	Time Interval	Mean	Variance	State Category
Sub-segment 1	0-120	2	1	1
Sub-segment 2	120-240	4	4	2
Sub-segment 3	240-360	8	16	3
Sub-segment 4	360-480	4	4	4
Sub-segment 5	480-600	2	1	5

As shown in the table, the statistical characteristics of the signal exhibit a typical high in the middle and low at both ends pattern: Segment 3 has the highest mean and variance, corresponding to large-amplitude vibration; Segments 1 and 5 have the lowest mean and variance, corresponding to weak vibration; and Segments 2 and 4 serve as transition stages. Together, they form a clearly non-stationary time-varying trend.

The sampling frequency is 10Hz, giving a total of N=6000 data points. Each of the five subsegments lasts 120s, causing the 600s response to exhibit gradually changing statistical properties over time. The original response time history and its state segmentation are shown in Fig. 7.

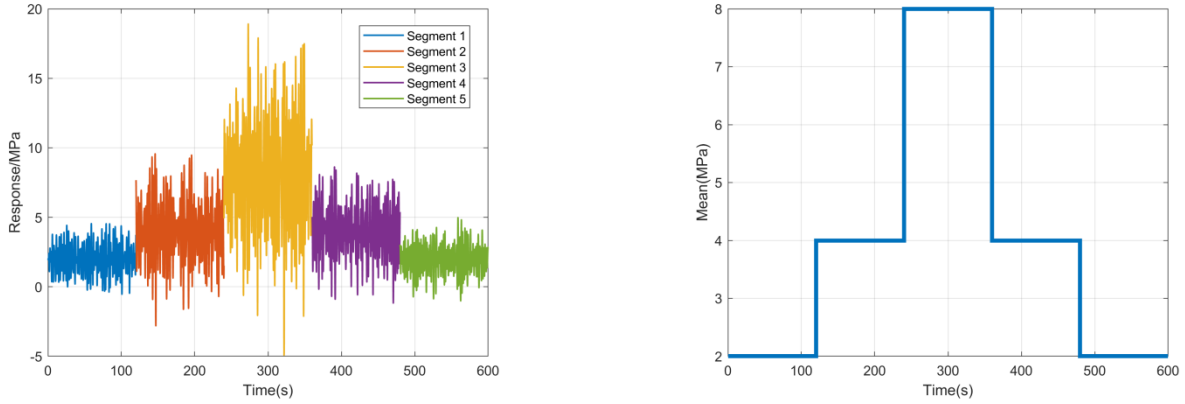

(a) Original response and its segmentation (b) Different stationary subsegments

Figure 7: Segmentation of Non-Stationary Response

Figure 7 presents the complete non-stationary response, showing a time-varying mean that changes stepwise over time. The significant variations in mean and variance indicate strong non-stationarity in the original signal and serve as an important source of large-amplitude transition cycles across states.

Because the statistical properties of the five segments are all different, the corresponding state sequence is $S(t) \in \{1,2,3,4,5,6,7,8,9\}$. Each state represents a statistically stable stationary subsegment. When the response transitions from segment k to segment $k+1$, abrupt changes in mean and variance occur, generating additional large-amplitude transition cycles in the stress series. The nine states appear sequentially and do not overlap. By traversing the state sequence once using adjacent sample pairs, the state transition counting matrix F can be obtained. Within each stationary subsegment, only the self-transition $k \to k$ occurs, repeated $L_k - 1$ times, while at the boundary between adjacent segments only a single transition $k \to k+1$ occurs. Thus, we obtain:

$$F=\begin{bmatrix} f_{11} & f_{12} & f_{13} & f_{14} & f_{15} \\ f_{21} & f_{22} & f_{23} & f_{24} & f_{25} \\ f_{31} & f_{32} & f_{33} & f_{34} & f_{35} \\ f_{41} & f_{42} & f_{43} & f_{44} & f_{45} \\ f_{51} & f_{52} & f_{53} & f_{54} & f_{55} \end{bmatrix}=\begin{bmatrix} L_1-1 & 1 & 0 & 0 & 0 \\ 0 & L_2-1 & 1 & 0 & 0 \\ 0 & 0 & L_3-1 & 1 & 0 \\ 0 & 0 & 0 & L_4-1 & 1 \\ 0 & 0 & 0 & 0 & L_5-1 \end{bmatrix} \tag{33}$$

Substituting the values $L_k=1200$ from this example, it can be further expressed as:

$$F=\begin{bmatrix} 1199 & 1 & 0 & 0 & 0 \\ 0 & 1199 & 1 & 0 & 0 \\ 0 & 0 & 1199 & 1 & 0 \\ 0 & 0 & 0 & 1199 & 1 \\ 0 & 0 & 0 & 0 & 1199 \end{bmatrix} \tag{34}$$

According to the definition of a Markov chain, the state transition probability matrix P can be obtained by normalizing each row of F, i.e.,

$$P=\begin{bmatrix} 0.9992 & 0.0008 & 0 & 0 & 0 \\ 0 & 0.9992 & 0.0008 & 0 & 0 \\ 0 & 0 & 0.9992 & 0.0008 & 0 \\ 0 & 0 & 0 & 0.9992 & 0.0008 \\ 0 & 0 & 0 & 0 & 1.0000 \end{bmatrix} \tag{35}$$

By directly applying the three-point rainflow counting method to the complete non-stationary response, the resulting cycle amplitude histogram and the three-dimensional rainflow spectrum are shown in Figure 8.

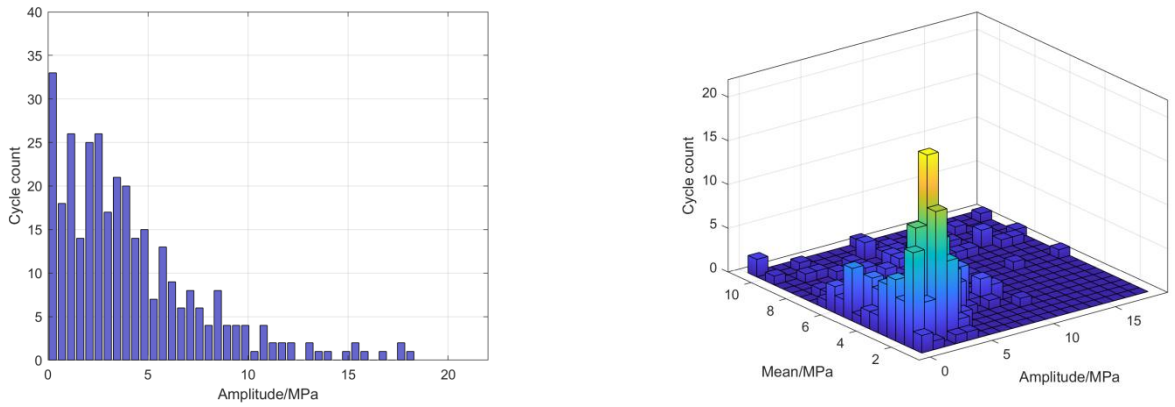

(a) Amplitude histogram (b) Rainflow cycle diagram

Figure 8: Traditional Rainflow Counting Method

Figure 8 presents the cycle amplitude distribution and the three-dimensional rainflow spectrum obtained by directly applying the traditional three-point rainflow counting method to the typical non-stationary response constructed in Example 2. The cycle amplitudes are mainly concentrated in the 0–15MPa range.

Using the TSD-RFC method, rainflow counting is first performed independently within each subsegment to obtain the intra-segment cycle spectrum, and then applied to the state-transition process to obtain the transition cycles. The complete cycle spectrum is finally synthesized, and its amplitude histogram and three-dimensional rainflow spectrum are shown in Figure 9.

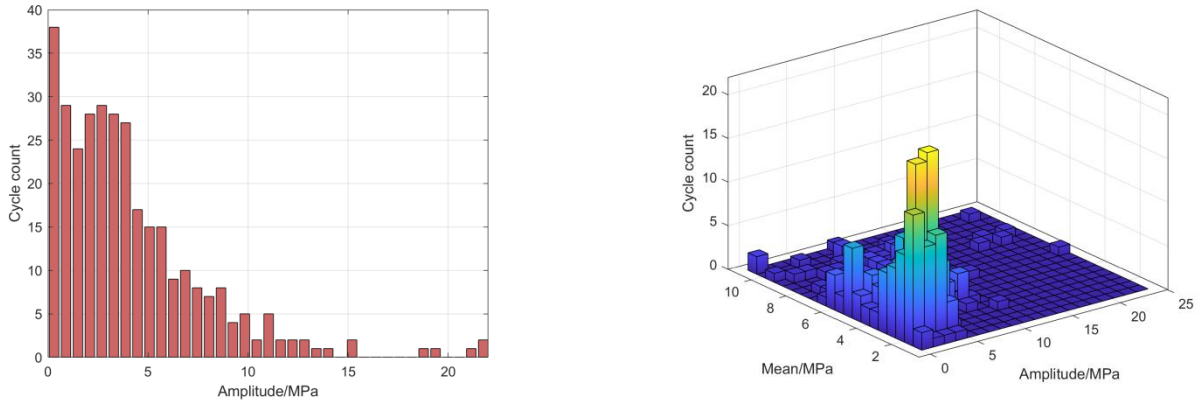

(a) Amplitude histogram (b) Rainflow cycle diagram

Figure 9: Dual-Layer Rainflow Counting Method

Figure 9 presents the cycle distribution obtained using the time-domain–state dual-layer rainflow counting method for the non-stationary response. Figure 8 (a) and 9 (a) compare the cycle amplitude histograms obtained by the traditional rainflow counting method and the dual-layer method in Example 2. The overall shapes are similar, but clear differences appear in the high-amplitude and medium–low-amplitude ranges. The dual-layer method processes the signal by segments and separately identifies state-layer cycles at switching points, preserving additional transition cycles generated by abrupt changes in mean and variance. These transition cycles usually have large amplitudes, leading to extra high-amplitude cycles in the dual-layer results.

In the medium–low amplitude range, the overall distributions remain consistent. The slight differences arise because the dual-layer method performs rainflow counting independently within each subsegment, causing minor changes in peak–valley pairing compared with whole-record processing. These differences are not methodological errors but a consequence of segmentation-induced peak–valley reorganization, and their quantity is small, having no substantial effect on the overall cycle characteristics.

Fig. 8 (b) and 9 (b) show the three-dimensional rainflow cycle diagrams obtained by the traditional and dual-layer methods. Overall, the cycle distributions in different regions remain largely consistent, both concentrated around an average stress of approximately 6MPa, with cycle counts gradually decreasing as amplitude increases. Differences appear mainly in the small- and high-amplitude ranges, for the same reasons discussed above.

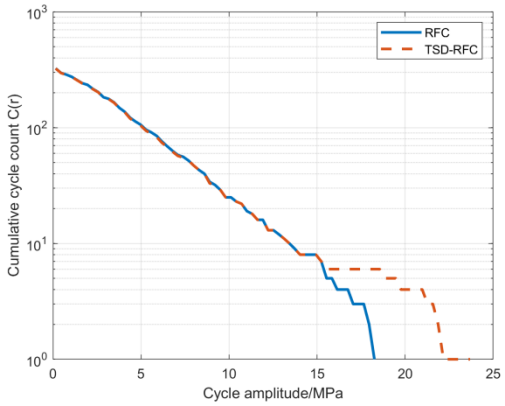

Figure 10: Comparison of Cumulative Stress Cycle Counts

Fig. 10 shows the cumulative stress cycle count curves C(r) obtained by the traditional rainflow counting method and the time-domain–state dual-layer rainflow counting method. Both curves exhibit a typical monotonically decreasing trend over the entire amplitude range, indicating overall consistency in cycle identification. However, slight but interpretable differences appear in the high-amplitude range, reflecting the different cycle mechanisms captured by the two counting approaches under non-stationary loading.

After completing the cycle identification using the traditional rainflow counting and the dual-layer rainflow counting methods, the cycles must be converted into quantitative indicators of structural fatigue response, with parameters referring to Section 3.1. The fatigue damage and fatigue life obtained by the two methods, as well as the fatigue contribution at different stress amplitudes, are shown in Fig. 11.

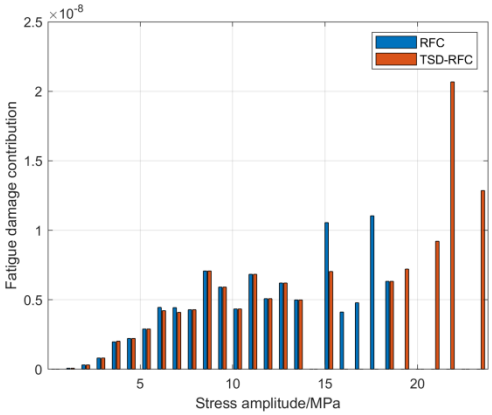

Figure 11: Comparison of Fatigue Damage Contributions

Fig. 11 presents the fatigue damage contributions of the traditional RFC and the TSD-RFC methods across different stress amplitude ranges. In the 2–14MPa range, the bar charts from the two methods are highly consistent, with only slight fluctuations. This is because TSD-RFC performs rainflow counting independently within each quasi-stationary segment, while the peak–valley structure inside each segment differs only minimally from whole-record processing and does not introduce additional fatigue error.

In the high-amplitude range, the fatigue damage predicted by TSD-RFC is noticeably higher than that from the traditional RFC. This occurs because the traditional RFC mixes abrupt transition points with neighboring extrema, making it difficult for them to form independent large cycles. In contrast, TSD-RFC identifies cross-segment transition cycles separately at the state layer, preserving these additional high-amplitude cycles. Although the number of tail cycles is small, their damage contribution is significant. The fatigue damage and life evaluations from both methods are summarized in Table 4.

Table 4. Fatigue Life Evaluation by Different Methods

Method	Fatigue Damage	Ratio	Fatigue Life	Variance
RFC	9.8×10^{-8}	1：1.16	1.02×10^{7}	1：0.863
TSD-RFC	1.14×10^{-7}		8.8×10^{6}	

Table 4 compares the total fatigue damage and corresponding equivalent fatigue life obtained by the traditional RFC and the TSD-RFC methods for Example 2. The damage ratio is approximately 1:1.16 and the life ratio is about 1:0.863, corresponding to differences of 16% and 14%, respectively.

At the junctions of time segments with different statistical characteristics, abrupt changes in the response mean and standard deviation generate spike-type large stress cycles. In the traditional method, pairing is performed within a unified peak–valley pool, so these abrupt variations are absorbed by surrounding local extrema and rarely form independent large cycles. In contrast, TSD-RFC explicitly identifies these transition cycles at the state layer. By decomposing the signal into quasi-stationary segments and introducing additional cycle identification at state-switching points, it captures high-amplitude cycles missed by the traditional approach. For high-cycle fatigue, the damage weight increases in a power-law manner with stress amplitude; therefore, even a small number of such cycles significantly affects the total damage. Hence, under typical non-stationary loading, TSD-RFC is necessary as a complement to the traditional RFC. The method improves cycle identification accuracy and provides a more robust basis for fatigue reliability assessment.

4. Fatigue Damage Study of Suspension Bridge Under Buffeting

4.1 Engineering Model and Dynamic Analysis

(1) Bridge Description

The engineering example considered in this study is a long-span suspension bridge located in a mountainous region. The main span of the bridge is 420m, and the total bridge length is 560m. Fig. 12 illustrates the general bridge layout and the cross-sectional configuration of the main girder.

The main girder adopts a steel truss stiffening-girder configuration with a total width of 13.3m and a girder height of 3.6m. The bridge deck consists of an 8m-wide traffic lane and two 1.5m-wide sidewalks. Due to the complex mountainous wind environment, the bridge is susceptible to significant non-stationary wind-induced vibration responses.

The global coordinate system is defined as follows: the X-axis represents the longitudinal bridge direction, the Y-axis represents the lateral bridge direction, and the Z-axis represents the vertical direction.The studied engineering case is a steel truss suspension bridge located in the mountainous region of western China, with a span of 420m. Specific dimensions are shown in the figure.

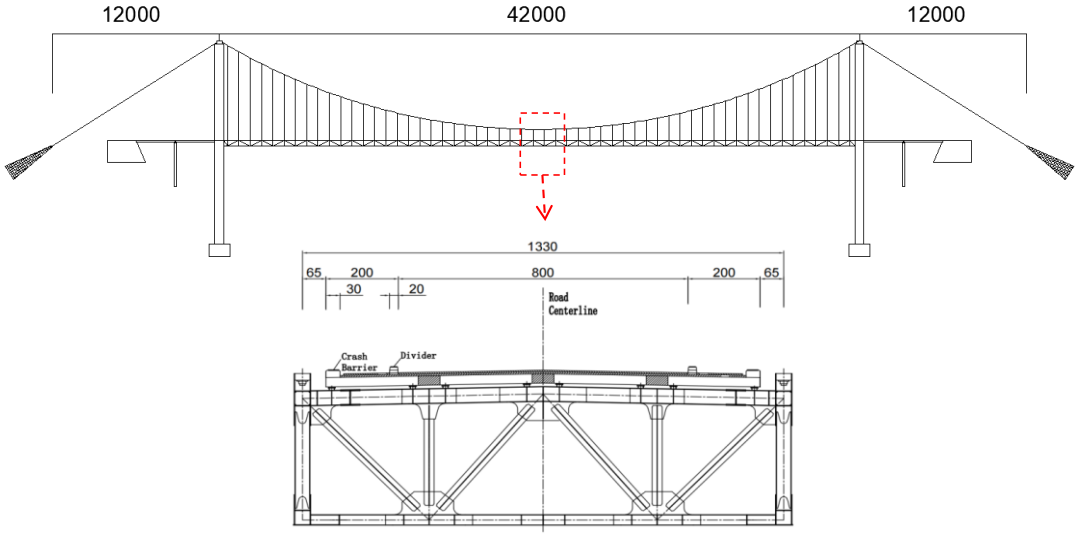

Figure 12: Suspension Bridge Elevation Diagram

(2) Finite Element Model

A three-dimensional finite element model of the suspension bridge was established in ANSYS for non-stationary buffeting and fatigue analysis, as shown in Fig. 13.

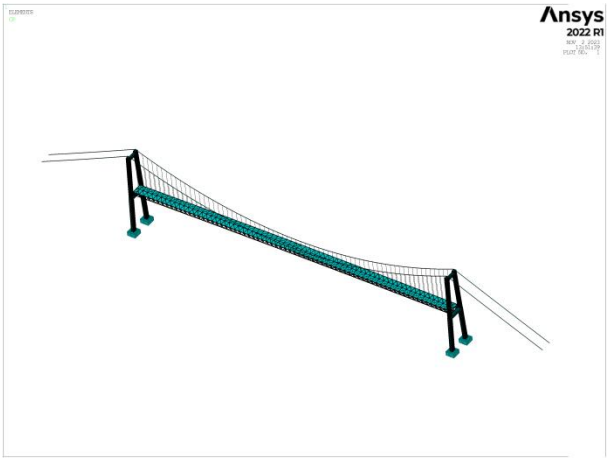

Figure 13: Finite Element Model

The bridge tower and stiffening girder were modeled using BEAM188 elements, while the main cables and hangers were simulated using tension-only LINK10 elements. The bridge deck was modeled using SHELL63 elements.

The finite element model was discretized according to the spatial layout of the bridge members. The stiffening girder was divided according to the truss panel points, and different beam sections were assigned to the upper chords, lower chords, web members, transverse beams, diaphragms, and wind bracing members. The main cables were discretized into cable elements between adjacent cable nodes, while the hangers were modeled as vertical tension members connecting the main cable and the stiffening girder. The bridge deck slab was meshed using shell elements connected to the girder nodes to ensure displacement compatibility.

The bridge tower was assumed to be constructed with C50 concrete, with an elastic modulus of 3.45×10^{10}Pa, density of 2420kg/m^3, and Poisson's ratio of 0.24. The stiffening girder adopted steel material properties with an elastic modulus of 2.06×10^{11}Pa, density of 7850kg/m^3, and Poisson's ratio of 0.30. The main cables were assigned an elastic modulus of 2.0×10^{11}Pa and a cross-sectional area of 0.09667m^2.

Rayleigh damping was adopted in the structural dynamic analysis, and the damping matrix was expressed as

$$C = \alpha M + \beta K \tag{36}$$

where M and K denote the structural mass and stiffness matrices, respectively, while α and β are the Rayleigh damping coefficients.

(3) Modal Characteristics and Boundary Conditions

The main girder was connected to the bridge towers through coupling constraints in the lateral (Y), vertical (Z), and rotational (ROTX) degrees of freedom. The main cables were fixed at the tower tops through the saddle system, while the side-span cable ends were anchored to the surrounding mountain rock mass. The tower bases were assumed to be fully fixed.

The corresponding boundary conditions are summarized in Table 5.

Table 5. The corresponding boundary conditions

Location	UX	UY	UZ	ROTZ	ROTX	ROTY
Tower–girder connection	Free	Fixed	Fixed	Free	Fixed	Fixed
Tower base	Fixed	Fixed	Fixed	Fixed	Fixed	Fixed
Main cable at tower top	Fixed	Fixed	Fixed	-	-	-
Side cable anchorage	Fixed	Fixed	Fixed	-	-	-

The first ten modal frequencies and corresponding modal characteristics of the structure are listed in Table 6. The modal results indicate that the bridge exhibits coupled lateral, vertical, torsional, and cable vibration characteristics, which are typical dynamic features of long-span suspension bridges under wind excitation.

Table 6. The first ten modal frequencies and corresponding modal characteristics

Modal order	Frequency /Hz	Modal shape
1	0.1821	1st symmetric horizontal vibration of main beam
2	0.2215	1st anti-symmetric vertical vibration of main beam
3	0.3127	1st symmetric vertical vibration of main beam
4	0.4091	2nd symmetric vertical vibration of main beam
5	0.4692	Main cable vibration
6	0.4843	Main cable vibration
7	0.5415	1st anti-symmetric torsional vibration of main beam
8	0.5855	Main cable vibration
9	0.5918	1st anti-symmetric torsional vibration of main beam
10	0.6093	1st anti-symmetric torsional vibration of main beam

(4) Stress Extraction Locations

To evaluate the fatigue-cycle characteristics under non-stationary buffeting, stress-response time histories were extracted from critical truss members located near the mid-span region of the stiffening girder, where relatively significant wind-induced stress fluctuations were observed.

The locations of the stress extraction elements are illustrated in Fig. 14. The selected members are sensitive to both local vibration responses and global state-transition-induced structural effects under non-stationary wind excitation.

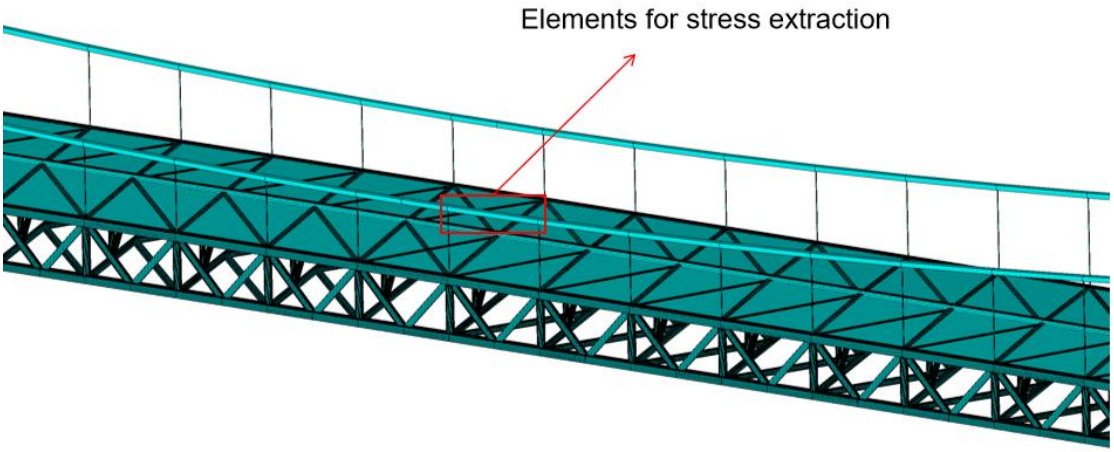

Figure 14: The Stress Extraction Location

This model has been previously validated in our prior paper(Hu et al., 2025), and further details will not be repeated here.

4.2 Non-Stationary Wind Field Simulation

The wind field is simulated using the harmonic synthesis method, with a simulation duration of 600s and a time interval of 0.25s. The Kaimal and Davenport spectra are used to simulate the along-wind and vertical turbulent wind speeds. The wind speed simulation points are uniformly distributed along the length of the main girder, with a total of 11 points, as shown in the figure.

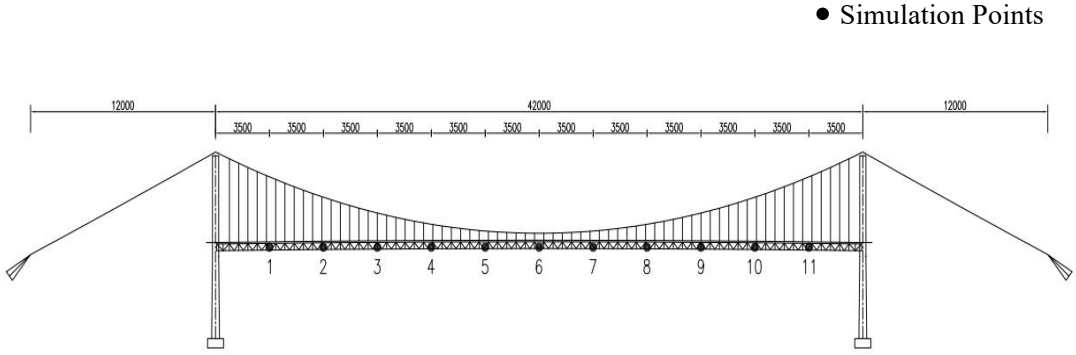

Figure 15: Simulation Point Loading Locations

The stationary wind field is converted into a non-stationary turbulent wind field using modulation functions, which are then combined with time-varying mean wind speed to form the non-stationary wind field. The formulas for the modulation function and the time-varying mean wind speed are as follows(Zhang et al., 2025):

$$A(t)=\exp\left(\frac{-(t-\alpha)^2}{\beta}\right) \tag{37}$$

$$\overline{U}(t)=U_{\max}d_m(t) \tag{38}$$

$$d_m(t)=\exp\left\{-\frac{(t-t_0)^2}{2D_t^2}\right\} \tag{39}$$

Where α =300, β =80000, and t_0 =300, D_t =600(Hu et al., 2025).

The time-varying mean wind speed and along-wind non-stationary turbulent wind speed are shown in the figure below:

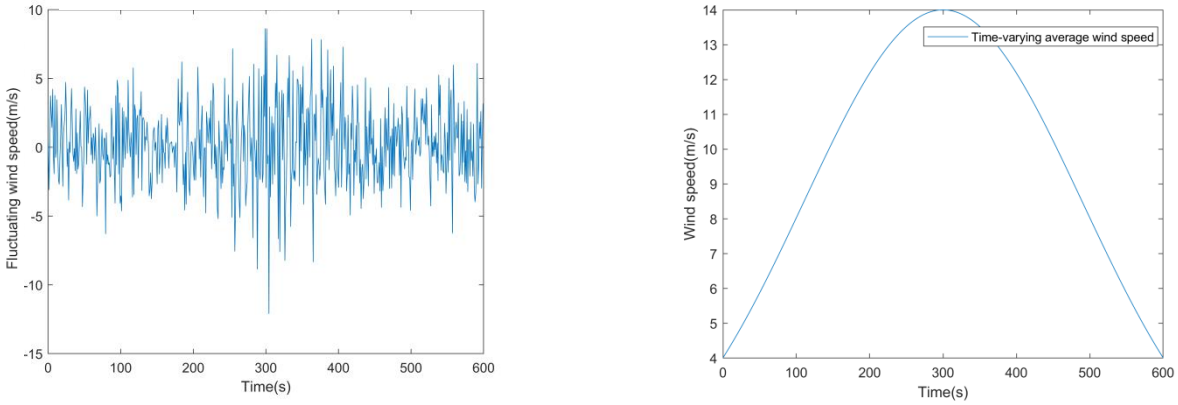

(a) Fluctuating Wind Speed (Along-Wind Direction) (b) Time-Varying Mean Wind Speed

Figure 16: Simulated Wind Speed

As shown in the figure, both the average wind speed and the non-stationary fluctuating wind speed exhibit time-varying characteristics. The time-varying power spectrum and the instantaneous power spectrum of the non-stationary fluctuating wind speed are illustrated as follows:

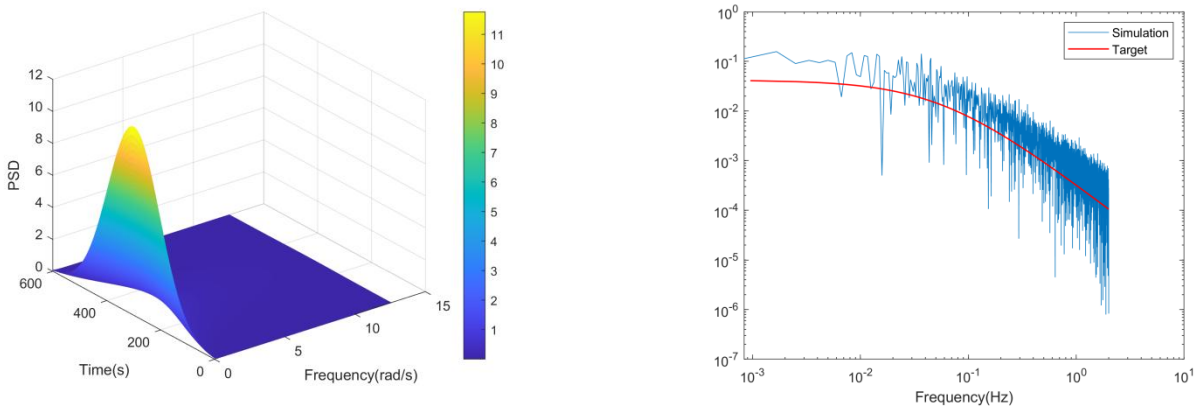

(a) Time-varying PSD (b) *t*=240 s

Figure 17: EPSD

The simulated wind field is applied to the model through the three components of the flutter force for flutter analysis, with the specific formula as follows:

$$\begin{aligned}
L_b(t)&=\frac{1}{2}\rho\overline{U}(t)B\left\{2C_L(\alpha_e)u(t)+\left[C_L'(\alpha_e)+C_D(\alpha_e)\right]w(t)\right\}\\
D_b(t)&=\frac{1}{2}\rho\overline{U}(t)B\left[2C_D(\alpha_e)u(t)+C_D'(\alpha_e)w(t)\right]\\
M_b(t)&=\frac{1}{2}\rho\overline{U}(t)B^2\left[2C_M(\alpha_e)u(t)+C_M'(\alpha_e)w(t)\right]
\end{aligned} \tag{40}$$

4.3 Fatigue Assessment Process

The fatigue assessment in the present study was performed based on the stress-response histories extracted from critical truss members of the stiffening girder under non-stationary buffeting excitation. Rainflow counting was employed to identify the stress cycles, and Miner's linear cumulative damage rule was adopted to evaluate the fatigue damage.

For each identified fatigue cycle, the stress amplitude was defined as

$$\Delta\sigma = \sigma_{\max} - \sigma_{\min} \tag{41}$$

where $\sigma_{\max}$ and $\sigma_{\min}$ denote the maximum and minimum stresses within the cycle, respectively.

Considering the influence of mean stress under asymmetric stress cycles, the Goodman fatigue limit model was adopted to convert the asymmetric stress cycles into equivalent stress amplitudes under symmetric loading conditions(Guan et al., 2026):

$$\Delta\sigma_{eq} = \frac{\sigma_b \Delta\sigma}{\sigma_b - \sigma_{\max} + \Delta\sigma/2} \tag{42}$$

where σ_b denotes the ultimate tensile strength of the steel wire, $\Delta\sigma$ is the stress range of the fatigue cycle, and $\sigma_{\max}$ is the maximum stress within the cycle.

The fatigue life corresponding to the equivalent stress amplitude was calculated using the adopted S–N relationship(Guan et al., 2026):

$$\lg \Delta\sigma_{eq} = 3.5305 - 0.0966 \lg\left(2N_f\right) \tag{43}$$

where $\Delta\sigma_{eq}$ is the equivalent stress amplitude and N_f is the number of cycles to failure.

The cumulative fatigue damage was calculated according to Miner's linear cumulative damage rule:

$$D = \sum_i \frac{n_i}{N_i} \tag{44}$$

where n_i and N_i represent the actual number of cycles and the allowable number of cycles corresponding to the i-th stress-amplitude level, respectively.

It should be noted that the fatigue damage obtained from the 600s non-stationary buffeting simulation is mainly used to characterize the relative short-term fatigue-damage characteristics under non-stationary wind excitation. The primary purpose of the present study is to investigate the influence of transition-induced cycles on fatigue-damage evaluation and the differences among various rainflow counting frameworks in identifying non-stationary fatigue cycles.

A complete long-term fatigue-life assessment would further require consideration of long-term wind-climate statistics, annual wind occurrence probabilities, long-term operational exposure duration, and cumulative effects under multiple wind environments. This issue will be further investigated in future work.

4.4 Component Fatigue Assessment

In this engineering case, the maximum damage to the main cable occurs under buffeting(Hu et al., 2025). Therefore, this study focuses on the fatigue damage of the main cable under the influence of a 10m/s non-stationary wind field. The stress response of the main cable under this wind speed condition and the segmentation of the stationary segments are shown in the figure.

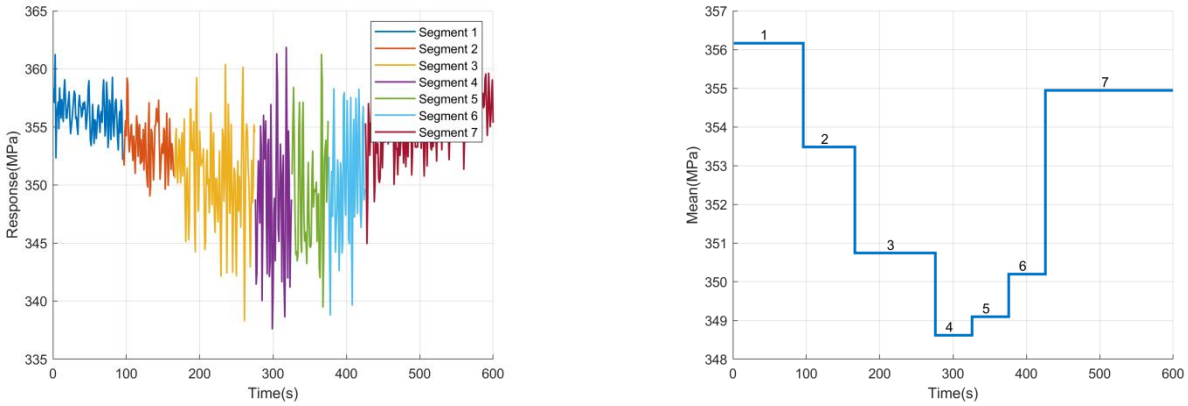

(a) Original response and its segmentation (b) Different stationary subsegments

Figure 18: Segmentation of Non-Stationary Buffeting

As shown in the figure, the response time history exhibits strong non-stationary characteristics, with different subsegments having varying mean values, the maximum difference being approximately 7.2MPa. If traditional rainflow counting is directly used for stress cycle statistics, the abrupt points at segment transitions will be absorbed by nearby local peaks and valleys, preventing the formation of independent large-amplitude cycles. Therefore, both the traditional rainflow counting method and the dual-layer rainflow counting method are applied to perform stress cycle statistics for the non-stationary response. The results are shown in the figure.

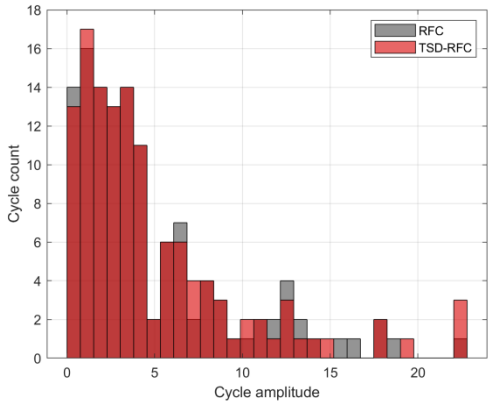

Figure 19: Comparison of Stress Cycle Values

It can be observed that in the lower amplitude stress cycle range, the two methods show little difference. However, in the high-amplitude stress cycle range, the dual-layer rainflow counting method yields higher values and a greater number of cycles compared to the traditional rainflow counting method. Based on the main cable's S-N curve, the difference in fatigue damage values between the two methods is calculated. The specific fatigue damage values for the main cable under different wind speed conditions are shown in the table below:

Table 5. Fatigue Damage Evaluation by Different Methods

Wind speed	Method	Fatigue damage
10m/s	RBF	1.72×10^{-9}
	TSD-RBF	1.87×10^{-9}
15m/s	RBF	8.4×10^{-9}
	TSD-RBF	9.19×10^{-9}
20m/s	RBF	3.6×10^{-8}
	TSD-RBF	4.01×10^{-8}

5. Conclusion

This study proposes a TSD-RFC method for accurately assessing the fatigue damage of suspension bridges under non-stationary wind loads. The proposed framework demonstrates that fatigue cycles in non-stationary responses are generated not only by local stochastic fluctuations within stationary states, but also by stochastic state transitions between different response regimes. This provides a new perspective for fatigue-cycle characterization under non-stationary wind-induced vibrations.

(1) The paper presents a dual-layer rainflow counting method that combines time-domain state segmentation with traditional rainflow counting. By decomposing the non-stationary response into multiple quasi-stationary segments, the classical rainflow counting method is applied within each segment, while state transition cycles are identified during the transition intervals, enabling precise identification of fatigue cycles under non-stationary wind loading.

(2) Through a comparison with traditional rainflow counting, the results show that the TSD-RFC method outperforms the traditional method in terms of accuracy. Particularly in high-amplitude stress cycles, TSD-RFC effectively distinguishes additional large-amplitude stress cycles caused by state transitions, whereas the traditional rainflow counting method

tends to merge these transition cycles with adjacent local peak-valley cycles, leading to incomplete cycle identification or misjudgment of amplitude.

(3) When evaluating the fatigue damage of the main cable under non-stationary wind loads on a suspension bridge, particularly at a wind speed of 20m/s, the TSD-RFC method results in significantly higher fatigue damage values compared to traditional rainflow counting. At a wind speed of 20m/s, the fatigue damage calculated by TSD-RFC increases by approximately 11.39%, indicating that the TSD-RFC method can more accurately identify and quantify the additional fatigue damage caused by wind speed fluctuations and state transitions, especially under high wind speed conditions.

Acknowledgements

This work did not receive any specific grant from funding agencies in the public, commercial, or not-for-profit sectors.

Data Availability: Research data is only available upon request

Editor: Rogério José Marczak

Reference:

Allard, L., & Snaiki, R. (2025). Buffeting-induced fatigue damage assessment of a long-span bridge under a changing climate scenario. Journal of Bridge Engineering, 30(3), 04024118.

Banday, Z. Z., Fenerci, A., Lystad, T. M., & Øiseth, O. A. (2025). Buffeting induced fatigue damage assessment of long-span bridge decks under uncertain turbulence conditions. Engineering Structures, 323, 119292.

Bibbo, N. D., Larsen, M. L., Baumgartner, J., & Arora, V. (2022). An improved rainflow counting method for multiaxial stress states using the minimum circumscribed circle method to identify shear stress ranges. International Journal of Fatigue, 163, 106997.

Chen, J., Imanian, A., Wei, H., Iyyer, N., & Liu, Y. (2020). Piecewise stochastic rainflow counting for probabilistic linear and nonlinear damage accumulation considering loading and material uncertainties. International Journal of Fatigue, 140, 105842.

Ding, Y., Ye, X. W., & Su, Y. H. (2025). Wind-induced fatigue life prediction of bridge hangers considering the effect of wind direction. Engineering Structures, 327, 119523.

Guan, J., Xue, H. J., & Chen, J. F. (2026). Research on High Fatigue Resistance and Life Prediction of 2200 MPa Main Cable Steel Wire. Modern Transportation and Metallurgical Materials, 6(02), 111-117.

Hu, J., Zhang, X., Tan, S., Liang, Y., & Wang, J. (2025). Fatigue damage analysis of steel truss suspension bridge under non-stationary and non-Gaussian buffeting. International Journal of Structural Stability and Dynamics, 25(06), 2550055.

Huang, G., Li, Y., Luo, Y., Xie, S., & Zhang, Y. (2023). One-stage extraction four-point algorithm for rainflow cycle counting in fatigue life estimation. Engineering Computations, 40(1), 126-148.

Jun, H., Xinqi, Z., Li, Z., Haibin, W., & Jiajian, W. (2025). Non-stationary characteristics of measured wind speed of continuous rigid frame bridge with high piers in mountains. Journal of Civil Structural Health Monitoring, 1-16.

Li, W., Cui, S., Zhao, J., An, L., Yu, C., Ding, Y., ... & Liu, Q. (2024). Experimental Study of Wind Characteristics at a Bridge Site in Mountain Valley Considering the Effect of Oncoming Wind Speed. Applied Sciences, 14(22), 10588.

Obermayr, M., Riess, C., & Wilde, J. (2021). A novel online 4-point rainflow counting algorithm for power electronics. Microelectronics Reliability, 120, 114112.

Pei, C., Bao, Y., Zhang, X., Cheng, X., & Feng, J. (2024). A CNN-LSTM model for predicting wind speed in non-stationary wind fields in mountainous areas based on wavelet transform and adaptive programming. AIP Advances, 14(11).

Su, Y. H., Wu, Y. R., & Sun, Q. (2022). Wind-Induced Response Analysis for a Fatigue-Prone Asymmetric Steel Arch Bridge with Inclined Arch Ribs. Advances in Materials Science and Engineering, 2022(1), 3489390.

Su, Y., Zeng, Y., & Han, G. (2025). Field measurement study of non-stationary wind events in a mountain valley: Focusing on two analysis strategies for turbulence characteristics. Journal of Wind Engineering and Industrial Aerodynamics, 267, 106266.

Thalla, O., & Stiros, S. C. (2018). Wind-induced fatigue and asymmetric damage in a timber bridge. Sensors, 18(11), 3867.

Wang, S., & Jia, J. (2024). Study on fatigue life of pc composite box girder bridge with corrugated steel webs under the combined action of temperature and static wind loads. Applied Sciences, 14(8), 3165.

Wang, X. W., Shang, D. G., Sun, Y. J., & Liu, X. D. (2019). Algorithms for multiaxial cycle counting method and fatigue life prediction based on the weight function critical plane under random loading. International Journal of Damage Mechanics, 28(9), 1367-1392.

Yuan, Z., Wang, H., Li, R., Mao, J., & Zong, H. (2025, March). Effect of displacement-controlled suspender on fatigue life of suspension structure under action of wind and traffic. Structures, 73, 108513.

Yuan, Z., Wang, H., Rou, L., Invernizzi, S., Mao, J., & Zong, H. (2025). Fatigue Life Evaluation of Suspenders on a Continuous Suspension Bridge Subject to Various Wind and Traffic Load Levels. INTERNATIONAL JOURNAL OF STRUCTURAL STABILITY & DYNAMICS, 26502901-265029032.

Zhang, X., Hu, J., Liang, Y., Yang, F., & Shen, A. (2025). Non-stationary buffeting response of suspension bridge in mountains based on time-varying power spectrum. Wind & structures, 41(1), 33-42.

Zhou, R., He, M., Cai, J., Zhou, H., Yang, Y., & Li, D. (2024). Non-stationary buffeting responses of a twin-box girder suspension bridge with various evolutionary spectra. Probabilistic Engineering Mechanics, 76, 103625.